ACS OMEGA

http://pubs.acs.org/journal/acsodf

Article

Development of the Cu/ZIF-8 MOF Acid-Sensitive Nanocatalytic Platform Capable of Chemo/Chemodynamic Therapy with Improved Anti-Tumor Efficacy

Jie Liang, Weiwei Zhang, Jun Wang, Wanzhen Li, Fei Ge, Weihao Jin, and Yugui Tao*

Cite This: *ACS Omega* 2023, 8, 19402−19412

Read Online

ACCESS | Metrics & More | Article Recommendations | Supporting Information

ABSTRACT: Recently, the combination of chemotherapy and chemodynamic therapy (CDT) has become a desirable strategy in the treatment of cancer. However, a satisfactory therapeutic outcome is often difficult to achieve due to the deficiency of endogenous H_2O_2 and O_2 in the tumor microenvironment. In this study, a CaO_2@DOX@Cu/ZIF-8 nanocomposite was prepared as a novel nanocatalytic platform to enable the combination of chemotherapy and CDT in cancer cells. The anticancer drug doxorubicin hydrochloride (DOX) was loaded onto calcium peroxide (CaO_2) nanoparticles (NPs) to form CaO_2@DOX, which was then encapsulated in a copper zeolitic imidazole ester MOF (Cu/ZIF-8) to form CaO_2@DOX@Cu/ZIF-8 NPs. In the mildly acidic tumor microenvironment, CaO_2@DOX@Cu/ZIF-8 NPs rapidly disintegrated, releasing CaO_2, which reacted with water to generate H_2O_2 and O_2 in the tumor microenvironment. The ability of CaO_2@DOX@Cu/ZIF-8 NPs to combine chemotherapy and CDT was assessed by conducting cytotoxicity, living dead staining, cellular uptakes, H&E staining, and TUNEL assays in vitro and in vivo. The combination of chemotherapy and CDT of CaO_2@DOX@Cu/ZIF-8 NPs had a more favorable tumor suppression effect than the nanomaterial precursors, which were not capable of the combined chemotherapy/CDT.

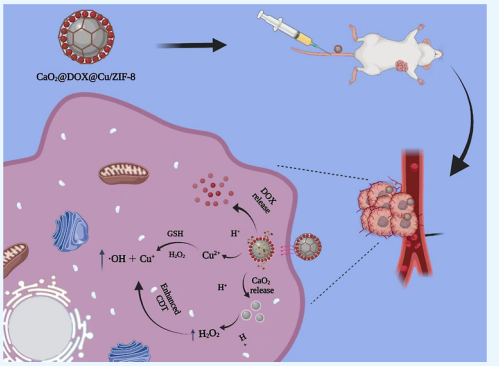

1. INTRODUCTION

Modulating oxidative stress in cancer cells is becoming an increasingly popular anticancer strategy. One method of modulating oxidative stress is through chemodynamic therapy (CDT), which relies on Fenton or Fenton-like reactions between metal ions and hydrogen peroxide (H_2O_2) to produce highly cytotoxic hydroxyl radicals ($^{\bullet}OH$) that induce oxidative stress in cells.[1] Therefore, CDT is particularly appealing as an anticancer strategy because it does not produce any off-target effects and can enhance the efficacy of traditional cancer treatments such as chemotherapy, photothermal therapy (PTT), and photodynamic therapy (PDT).[1−4] However, the Fe^{2+} that catalyzes the Fenton reaction reacts weakly with H_2O_2 under weakly acid conditions, such as in the tumor microenvironment, and is only effective under strongly acidic conditions with pH values up to 2−4.[5−8] In contrast, Cu^{+} can generate hydroxyl radicals ($^{\bullet}OH$) more efficiently than Fe^{2+} through Fenton-like reactions under weakly acidic or neutral conditions. Furthermore, Cu^{+}-catalyzed Fenton-like reactions are approximately 160 times faster than those catalyzed by Fe^{2+}.[9,10]

Recently, copper-containing MOFs have attracted significant interest in cancer therapy due to their unique physicochemical properties and excellent biocompatibility, as well as their ability to easily control the structure, composition, morphology, and size of the MOFs during preparation. In addition, the organic ligands in the MOFs do not prevent the Cu^{2+} ions from producing hydroxyl radicals ($^{\bullet}OH$) through Fenton-like reactions with H_2O_2, and the MOFs can be loaded with chemotherapeutic drugs for enabling tumor chemotherapy due to their large specific surface areas. For example, MOF199, a copper-based MOF, has been used as a nanocarrier for drug delivery.[9,11−14] However, reports on the application of copper-based MOFs for CDT therapy are still scarce, despite their widespread potential as novel therapeutics for the treatment of a variety of different cancers.[15]

The therapeutic efficacy of CDT is highly dependent on the levels of endogenous H_2O_2 in the tumor microenvironment.[16,17] Although most tumor cells contain significantly higher levels of intracellular H_2O_2 compared to normal cells, these levels are still not sufficient for effective CDT treatment of tumor cells.[18] Therefore, the ability of a CDT agent to generate enough H_2O_2 for inducing oxidative stress is critical for ensuring that it exhibits robust anti-cancer potency. This problem can be circumvented by incorporating compounds

Received: January 20, 2023
Accepted: May 11, 2023
Published: May 26, 2023

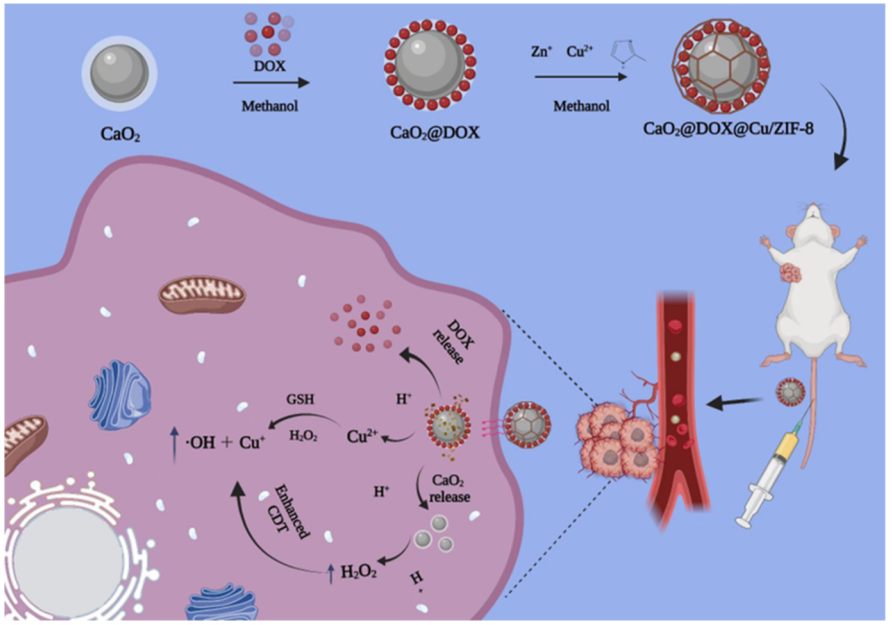

Figure 1. Synthesis of CaO_2@DOX@Cu/ZIF-8. Anti-tumor mechanism of CaO_2@DOX@Cu/ZIF-8 in vivo.

capable of generating intracellular H_2O_2 into drug delivery systems.[19] To improve the efficacy of CDT, materials can be developed that enable a combination of chemotherapy, PDT, PTT, and other therapeutic mechanisms to overcome the hurdles from which individual therapeutic mechanisms often suffer.[20−23] Doxorubicin hydrochloride (DOX) is a well-known and highly utilized chemotherapeutic drug in cancer treatment.[24,25] Under aerobic conditions, DOX can activate nicotinamide adenine dinucleotide phosphate (NADPH) oxidase, which catalyzes the reaction between NADPH and O_2 to generate superoxide radicals ($O_2^{\bullet-}$).[26] Superoxide dismutase (SOD) can convert $O_2^{\bullet-}$ to H_2O_2, which is the substrate of CDT.[27] In cancer cells, the production of $O_2^{\bullet-}$ will induce oxidative damage, leading to apoptosis.[28] However, because most tumor microenvironments are O_2-deficient, the ability of DOX to generate $O_2^{\bullet-}$ in tumor cells will be limited.[29] Therefore, circumventing the O_2 deficiency problem of the tumor microenvironment can improve the sensitivity of tumor cells to DOX while also improving CDT efficacy.

Exogenous calcium peroxide (CaO_2) has demonstrated the ability to provide the tumor microenvironment with enough H_2O_2 and O_2 to promote CDT.[30] CaO_2 also has excellent biocompatibility and will not cause toxic side effects in normal cells after entering the body.[31] Upon entering the tumor microenvironment, CaO_2 reacts with water to produce H_2O_2 and O_2.[32−35] However, since CaO_2 reacts readily with water, finding a suitable carrier to ensure that CaO_2 will not break down prematurely before entering tumor cells is imperative. Herein, as shown in Figure 1, we designed a MOF comprising a copper zeolitic imidazolate framework (Cu/ZIF-8) that was loaded with DOX and CaO_2. The Cu/ZIF-8 was chosen because it is stable under physiologically neutral conditions, thereby preventing DOX and CaO_2 from disassociating from the MOF due to decomposition.[36,37] To prepare the MOF nanocomposite, CaO_2 nanoparticles (NPs) were first synthesized, after which DOX was loaded onto the surface of CaO_2 NPs to form CaO_2@DOX. Finally, the CaO_2@DOX surface was modified with a layer of Cu/ZIF-8 to synthesize CaO_2@DOX@Cu/ZIF-8. We hypothesized that, upon entering the acidic microenvironment of the tumor, the Cu/ZIF-8 framework will rapidly decompose to release DOX, CaO_2, and Cu^{2+}, the latter of which catalyzes the Fenton-like reactions to produce H_2O_2 in situ. Meanwhile, the unprotected CaO_2 will react with water to form H_2O_2 and O_2. In the presence of excess GSH in the tumor microenvironment, the generated H_2O_2 will react with the dissociated Cu^{2+} in a Fenton-like reaction to produce highly toxic $^{\bullet}OH$. Furthermore, the generated O_2 will improve the hypoxic condition within the tumor, enhance the sensitivity of the tumor cells to DOX, and improve the efficacy of the chemotherapy. Therefore, the independent production of both H_2O_2 and O_2 by the MOF nanocomposite will enable a synergistic CDT and chemotherapeutic effect, offering a new strategy to improve the effectiveness of combinatorial chemokinetic therapies.

2. EXPERIMENTAL SECTION

2.1. Materials. Anhydrous calcium chloride ($CaCl_2$), ammonium hydroxide ($NH_3{\cdot}H_2O$, 28 wt %), polyethylene glycol 200 (PEG-200), hydrogen peroxide (H_2O_2, 30 wt %), DOX, 2-methylimidazole (99%), copper(II) nitrate trihydrate ($Cu(NO_3)_2{\cdot}3H_2O$, 99.5%), zinc nitrate hexahydrate ($Zn(NO_3)_2{\cdot}6H_2O$, 98%), triethylamine (>98%), and methanol (99.5%) were obtained from Aladdin Reagents (Shanghai, China). 1,3-Diphenylisobenzofuran (DPBF), 2′,7′-dichlorofluorescin diacetate (DCFH-DA), and 5,5′-dithiobis-(2-nitrobenzoic acid) (DTNB) were obtained from Nanjing KGI Biotechnology Development Co., Ltd. Roswell Park Memorial Institute-1640 (RPMI-1640), phosphate buffered saline (PBS), fetal bovine serum (FBS), penicillin−streptomycin (cell culture-grade), and trypsin (0.25%) containing 0.1% ethylenediaminetetraacetic acid (EDTA) were purchased from Servicebio Co., Ltd. The Calcein AM/PI Double Stain Kit, Annexin V-FITC/PI Apoptosis Detection Kit, and Cell Counting Kit-8 (CCK-8) were obtained from Nanjing KGI Biotechnology Development Co., Ltd. HGC cells were obtained from Procell Life Science and Technology Co., Ltd.

2.2. Preparation of CaO_2@DOX@Cu/ZIF-8 NPs. *2.2.1. Synthesis of CaO_2.* First, $CaCl_2$ (2 g) was dissolved in

https://doi.org/10.1021/acsomega.3c00269
ACS Omega 2023, 8, 19402−19412

distilled water (15 mL), to which $NH_3{\cdot}H_2O$ (10 mL of a 1 mol/L solution diluted from the 28 wt % concentrate) and PEG-200 (100 mL) were added sequentially. H_2O_2 (15 mL of 30 wt % solution) was added dropwise to the solution while stirring over 20 min to form a precipitate, which was collected by centrifugation (12,000 rpm, 15 min), washed three times with methanol, and dried under a vacuum at 60 °C for 4 h.

2.2.2. Synthesis of CaO_2@DOX. First, CaO_2 (50 mg) was dissolved in methanol (40 mL) by ultrasonication. Then, 10 mL of a 1 mg/mL solution of DOX in methanol was added to the solution, which was stirred for 10 h. After centrifugation of the mixture (12,000 rpm, 15 min), the pellet was washed three times with methanol and dried under vacuum at 60 °C for 4 h to obtain CaO_2@DOX.

2.2.3. Synthesis of CaO_2@DOX@Cu/ZIF-8. CaO_2@DOX@Cu/ZIF-8 was prepared by an in situ assembly method. First, CaO_2@DOX (50 mg) was dispersed into methanol (20 mL) under ultrasonication. Separately, $Zn(NO_3)_2{\cdot}6H_2O$ (12 mg) and $Cu(NO_3)_2{\cdot}3H_2O$ (3 mg) were dissolved in methanol (10 mL). Then, in another container, 2-methylimidazole (13 mg) was dissolved in methanol (10 mL), to which triethylamine (16 μL) was added dropwise. Finally, all three solutions were mixed and stirred at room temperature for 2 h. The product was collected by centrifugation (12,000 rpm, 15 min), washed three times with methanol, and dried under a vacuum at 60 °C for 4 h.

2.3. Characterization of CaO_2@DOX@Cu/ZIF-8. The scanning electron microscope used to characterize the morphological structure of the material was purchased from Hitachi, Japan. A UV−vis spectrophotometer (Shanghai Metash Instruments Co.) was employed to characterize the changes in absorbance during the synthesis of the materials. Fourier-transform infrared spectroscopy (FT-IR, Thermo Scientific, USA) was used to characterize the functional groups in the various materials. A particle size analyzer (Brookhaven Instruments, USA) was used to measure the zeta potentials and particle sizes of the materials. Lastly, flow cytometry (Beckman Coulter, USA) and fluorescence microscopy (Olympus, Japan) were employed for in vitro cell analysis.

2.4. Kinetics of DOX Release from CaO_2@DOX@Cu/ZIF-8. Since the pH of an environment affects the rate of drug release, the kinetics of DOX release from CaO_2@DOX@Cu/ZIF-8 was simulated in physiological environments with pH values of 5.5 and 7.4. CaO_2@DOX@Cu/ZIF-8 was dissolved in 2 mL of PBS (pH 5.5 and 7.4), and the solutions were sealed in dialysis bags (2000 kDa cutoff). The dialysis bags were immersed in 30 mL of PBS at 37 °C in the dark, and aliquots (2 mL) of the solution were removed at regular intervals to quantitate the amount of DOX in solution based on the change in absorbance at 480 nm.

2.5. ROS Detection and GSH Consumption. The $^{\bullet}OH$ generation performance of CaO_2@DOX@Cu/ZIF-8 NPs was investigated using DPBF as an $^{\bullet}OH$ quencher. DPBF reacts with $^{\bullet}OH$ in solution, resulting in a reduction in the absorbance at 410 nm. We prepared two sets of CaO_2@DOX@Cu/ZIF-8 (1 mg/mL) aqueous solutions (3 mL): one set containing 1 mL of GSH (20 mM) as the experimental group and the other set adding no more than 1 mL of GSH-free distilled water as the control group. H_2O_2 (1 mL of a 1 mM solution) and DPBF (1 mL of a 10 mg/mL solution) were added to each solution, and the changes in the absorbance of CaO_2@DOX@Cu/ZIF-8 solutions (with and without GSH) as a result of DPBF were measured by UV−vis spectroscopy.

DTNB was employed to study the responsiveness of CaO_2@DOX@Cu/ZIF-8 to GSH. First, 240 μL of a 2.5 mg/mL solution of DTNB in PBS and 30 μL of a 9.4 mM solution of GSH in water were added to deionized water (2 mL). This solution was diluted with CaO_2@DOX@Cu/ZIF-8 NPs (200 μg/mL) to achieve final concentrations of CaO_2@DOX@Cu/ZIF-8 NPs of 0, 10, 20, 40, and 80 μg/mL, while maintaining the same volume across all five solutions. The solutions were allowed to stand for 30 min, after which they were centrifuged (10,000 rpm, 10 min), and the absorbance of the supernatant was measured by UV−vis spectroscopy at 412 nm.

2.6. Cytotoxicity. HGC cells were cultured in a medium comprising 89% RPMI-1640, 10% FBS, and 1% penicillin−streptomycin in an incubator set at 37 °C with a CO_2 concentration of 5%. The survival rate of cells treated with CaO_2@DOX@Cu/ZIF-8 NPs was determined by CCK-8 assays. The HGC cells were inoculated into 96-well plates (1×10^4 cells/well). Free DOX (0.625, 1.25, 2.5, 5, and 10 μg/mL) as well as CaO_2@Cu/ZIF-8 and CaO_2@DOX@Cu/ZIF-8 (12.5, 25, 50, 100, and 200 μg/mL each) were added to the cell suspensions. After incubating for 24 h, the cells were washed twice with 100 μL of PBS, after which 10 μL of the CCK-8 reagent was added, and the cells were incubated for 2 h in the dark. Finally, the absorbance of each solution was measured at 450 nm using a microplate reader to calculate the cell viability.

2.7. Intracellular $^{\bullet}OH$ Detection. HGC cells were inoculated into 6-well plates (1×10^5 cells/well) and cultured at 37 °C with a CO_2 concentration of 5%. All materials were dissolved in medium. Each solution in each well was supplemented with 2 mL of DOX (5 μg/mL), 2 mL of Cu/ZIF-8 NPs (100 μg/mL), and 2 mL of CaO_2@DOX@Cu/ZIF-8 NPs (100 μg/mL), and the cells were incubated for 6 h. After washing the cells twice with 100 μL of PBS each, 2 mL of DCFH-DA (10 μM) was added, and the cells were incubated for another 30 min. After incubation, the HGC cells were washed twice with 100 μL of PBS and observed under a fluorescent microscope. In addition, 2 mL of CaO_2@DOX@Cu/ZIF-8 NPs (100 μg/mL) were added to HGC cells and then incubated for 0, 2, 4 and 6 h. The cells were treated according to the same operation as above, and the results of the experiment were observed again.

2.8. Cellular Uptake and Apoptosis Assays. HGC cells were inoculated into 6-well plates (1×10^5 cells/well). The culture environment temperature was 37 °C, and the CO_2 concentration was 5%. HGC cells without material treatment were used as the control (blank). The HGC cells in the experimental group were supplemented with 2 mL of a 50 μg/mL solution of CaO_2@DOX@Cu/ZIF-8 and incubated for 2, 6, and 12 h. After 12 h, the HGC cells were fixed with ice methanol for 0.5 h, and the pellet was washed twice with PBS. The HGC cells nuclei were labeled by DAPI and observed under a fluorescence microscope. The changes in fluorescence of DOX after cellular uptake of the MOF nanocomposite were quantified by flow cytometry.

The effect of free DOX, CaO_2@Cu/ZIF-8, and CaO_2@DOX@Cu/ZIF-8 on inducing apoptosis was assessed in HGC cells. The cells without material treatment represented the control (blank). The HGC cells in the experimental group were separately treated with free DOX (5 μg/mL), CaO_2@Cu/ZIF-8 (100 μg/mL), and CaO_2@DOX@Cu/ZIF-8 (100 μg/mL), and the cells were incubated for 24 h. The HGC cells were collected from 6-well plates after digestion with trypsin

https://doi.org/10.1021/acsomega.3c00269
ACS Omega 2023, 8, 19402−19412

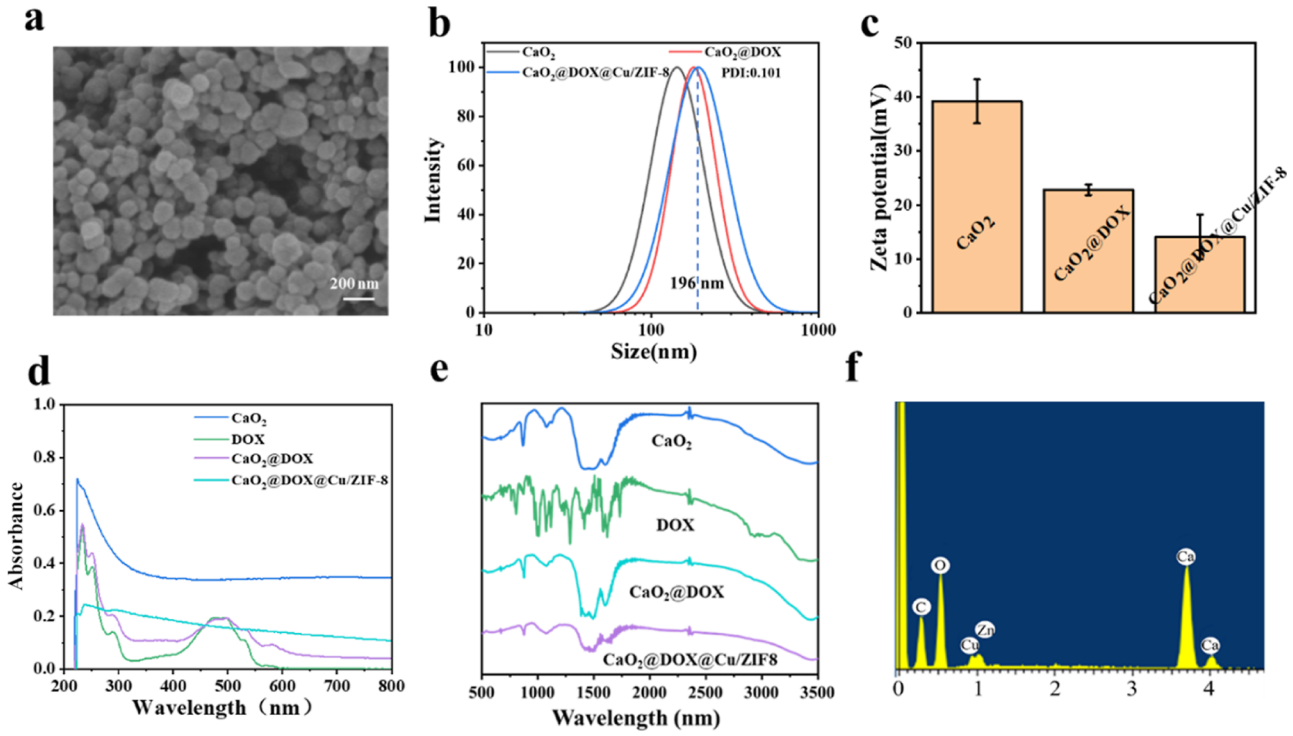

Figure 2. Characterization of CaO_2@DOX@Cu/ZIF-8 NPs. (a) SEM images and (b) DLS particle size analysis of CaO_2@DOX@Cu/ZIF-8. (c) Zeta potentials of CaO_2, CaO_2@DOX, and CaO_2@DOX@Cu/ZIF-8. (d) UV−vis spectra of CaO_2, DOX, CaO_2@DOX, and CaO_2@DOX@Cu/ZIF-8. (e) FTIR spectra of CaO_2, DOX, CaO_2@DOX, and CaO_2@DOX@Cu/ZIF-8. (f) Energy spectra of Ca, Zn, Cu, C, and O in CaO_2@DOX@Cu/ZIF-8.

and centrifugation (500 rpm, 24 °C, 5 min), and the pelleted cells were reconstituted in 500 μL of binding buffer after washing twice with pre-chilled PBS. Finally, the cells were stained with 5 μL of Annexin V-FITC and PI to determine the apoptotic status by flow cytometry.

2.9. Live−Dead Staining Assay. HGC cells were inoculated into 6-well plates (1×10^5 cells/well). The culture environment temperature was 37 °C, and the CO_2 concentration was 5%. HGC cells were separately treated with 2 mL of free DOX (10 μg/mL), 2 mL of CaO_2@Cu/ZIF-8 (200 μg/mL), and 2 mL of CaO_2@DOX@Cu/ZIF-8 (200 μg/mL). After 24 h of incubating, the HGC cells were washed with PBS twice, after which they were stained with 2 mL of PI and Calcein-AM (5 μg/mL). After incubation at 37 °C for 20 min in the dark, cells were washed twice with PBS and then analyzed by fluorescence microscopy.

2.10. In Vivo Analysis. BALB/c female nude mice (about 4 weeks old, Nanjing Marex Biotechnology Co., Ltd.) were kept in a sterile room at a temperature of 26 °C and 40−50% relative humidity. All animal procedures were performed in accordance with the guidelines for care and use of Laboratory Animals of Soochow University and approved by the Soochow University Laboratory Animal Center (approval number: 202210A415). HGC cells ($1-2 \times 10^6$) were suspended in 100 μL of PBS and inoculated into the axilla of the nude mice for seven consecutive days to establish an in vivo mouse tumor model. After the tumors reached a certain size, the mice were divided into four treatment groups ($n = 3$): the PBS group (control), the DOX group, the CaO_2@Cu/ZIF-8 group, and the CaO_2@DOX@ZIF-8 group. The individual treatments were administered into the caudal vein (tail) (the drug injection dose was calculated as 2 mg/kg dissolved in 200 μL of PBS) for 14 consecutive days, and the tumor volumes and changes in body weight of the mice were recorded daily. After the 14 day treatment period, the nude mice were sacrificed, and the heart, liver, spleen, lungs, kidneys, and tumor were dissected. The excised hearts, livers, spleens, lungs, kidneys, and tumors were preserved in formalin for subsequent histological analysis. Sections of these organs and tumors were also stained with hematoxylin and eosin (H&E) stain, and the tumors were examined for apoptosis by the TUNEL method.

3. RESULTS AND DISCUSSION

3.1. Characterization of CaO_2@DOX@Cu/ZIF-8 NPs. A bottom-up approach was used to synthesize CaO_2@DOX@Cu/ZIF-8 NPs. First, CaO_2 was prepared by a hydrolysis-precipitation method. DOX was then immobilized on the surface of CaO_2 through coordination bonds between DOX and Ca^{2+} to form CaO_2@DOX. The Cu/ZIF-8 was then fabricated on the surface of CaO_2@DOX using an in situ synthesis approach to prepare CaO_2@DOX@Cu/ZIF-8 NPs. scanning electron microscopy (SEM) images of CaO_2@DOX@Cu/ZIF-8 (Figure 2a) show that the nanocomposite particles were spherical in shape and were ∼200 nm in diameter (Figure 2b). The zeta potential of CaO_2 was +39.17 mV (Figure 2c), but after the surface of CaO_2 was coated with DOX, the zeta potential decreased to +22.80 mV, indicating that DOX was successfully loaded with CaO_2. After wrapping Cu/ZIF-8 around CaO_2@DOX, the zeta potential decreased to +14.6 mV, indicating that the Cu/ZIF-8 was successfully loaded onto CaO_2@DOX NPs.

Figure 2d shows that the UV−vis spectrum of CaO_2@DOX featured the same absorption peak around 490 nm as the UV−vis spectrum of pure CaO_2, indicating the successful loading of

https://doi.org/10.1021/acsomega.3c00269
ACS Omega 2023, 8, 19402−19412

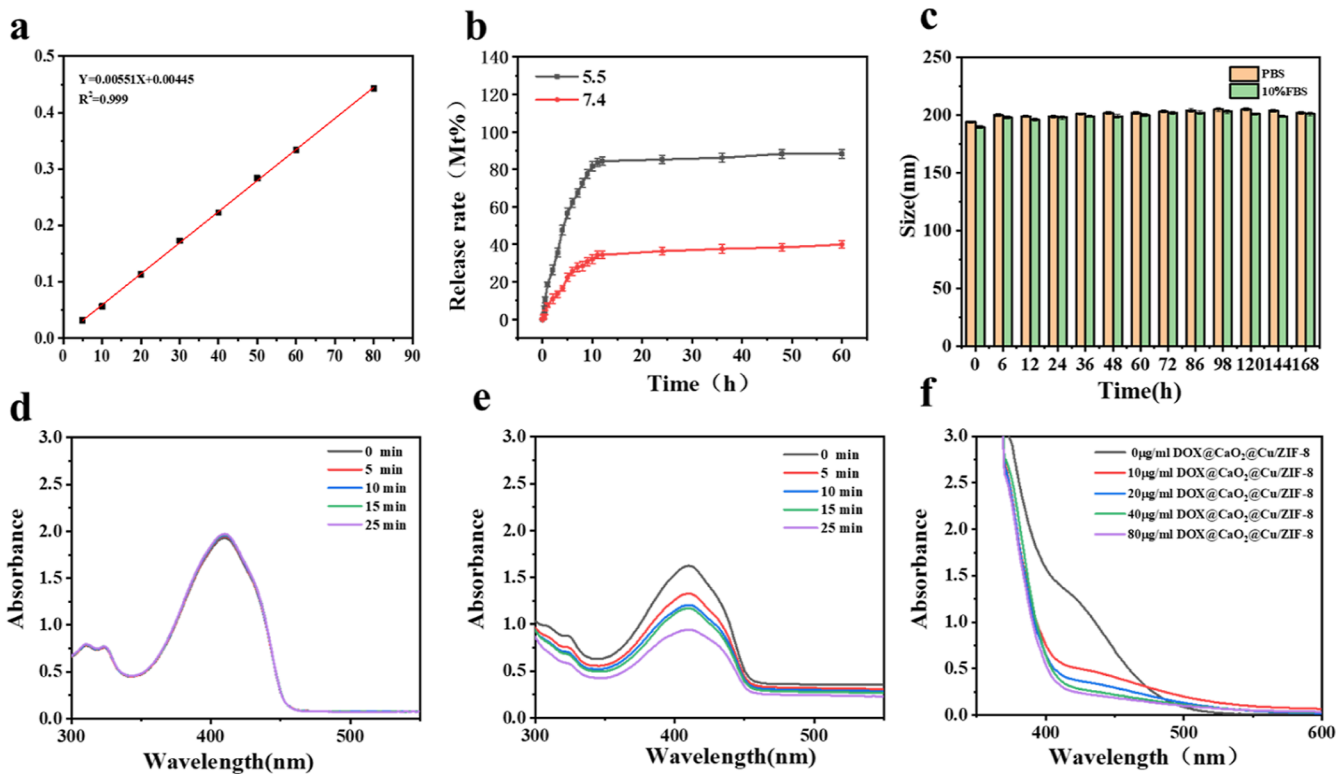

Figure 3. Characterization of CaO_2@DOX@Cu/ZIF-8. (a) DOX standard curve. (b) Drug release profiles of CaO_2@DOX@Cu/ZIF-8 at different pHs. (c) Changes in the particle size of CaO_2@DOX@Cu/ZIF-8 NPs in PBS (pH 7.4) and FBS. (d) Production of ROS by CaO_2@DOX@Cu/ZIF-8 under normal physiological conditions. (e) Production of ROS by CaO_2@DOX@Cu/ZIF-8 in a simulated tumor microenvironment. (f) GSH depletion capacity at different concentrations of CaO_2@DOX@Cu/ZIF-8 (0, 10, 20, 40, and 80 μg/mL).

DOX onto CaO_2. However, the absorption spectrum of CaO_2@DOX@Cu/ZIF-8 did not feature the peak at 490 nm, indicating that the Cu/ZIF-8 had been successfully wrapped around CaO_2@DOX. FT-IR was utilized to further assess whether CaO_2@DOX@Cu/ZIF-8 was successfully prepared by analyzing the changes in the functional groups throughout the preparation. As shown in the FT-IR spectrum of CaO_2, DOX, CaO_2@DOX, and CaO_2@DOX @ Cu/ZIF-8 (Figure 2e), the absorption bands at 881 and 1115 cm^{-1} corresponded to the characteristic peaks of peroxide bonds (O−O), indicating that CaO_2 was successfully prepared. The FT-IR spectrum of DOX featured absorption bands at 987, 1211, 1284, 1406, 1618, and 3421 cm^{-1}, which corresponded to the N−H stretching vibrations, C−O−C stretching vibrations, C═N stretching vibrations, C−H bending vibrations, C═O stretching vibrations, and O−H stretching vibrations, respectively. The FTIR spectra of CaO_2@DOX and CaO_2@DOX@Cu/ZIF-8 featured the same vibrational peaks as DOX near 1406 cm^{-1}, indicating that the DOX was successfully loaded onto CaO_2. CaO_2@DOX@Cu/ZIF-8 produced the same characteristic peak at 1584 cm^{-1} as ZIF-8, indicating that Cu/ZIF-8 was successfully loaded onto CaO_2@DOX NPs. Figure 2f shows the elemental mapping of CaO_2@DOX@Cu/ZIF-8, which demonstrated that the nanocomposite comprised Ca, O, Zn, and Cu elements that were uniformly distributed throughout.

The loading of DOX and the release kinetics of DOX from CaO_2@DOX@Cu/ZIF-8 were analyzed by UV−vis spectrophotometry. According to the standard curve (Figure 3a), the loading capacity of DOX was quantitatively determined to be 5.0 wt %. At pH 7.4, the cumulative DOX release was only 30% (Figure 3b). However, when the pH dropped to 5.5, more than 90% of the total DOX was released within 15 min. These results corroborated the hypothesis that the Cu/ZIF-8 framework would decompose under acidic conditions, achieving an efficient release of DOX. To ensure that the pH of the solution did not affect the shape and stability of the MOF nanocomposite, the particle size analyzer was used to monitor the stability of CaO_2@DOX@Cu/ZIF-8 in serum and PBS (pH = 7.4). After 168 h in both serum and PBS, the particle size of the material negligibly changed, indicating that it would be highly stable under physiological conditions (Figure 3c).

3.2. Detection of Extracellular •OH. The ability of CaO_2@DOX@Cu/ZIF-8 to generate H_2O_2 radicals was investigated using the fluorescent probe DPBF. DPBF has long been recognized for its high specificity in reacting with reactive oxygen species (ROS), such as hydroxyl (•OH), alkoxy (RO•), or alkylperoxy (ROO•) radicals. Upon reaction with these ROS, DPBF is rapidly converted to 1,2-dibenzoylbenzene (DBB) and irreversibly oxidized, causing its absorption intensity at 410 nm to be rapidly reduced. In the tumor microenvironment, CaO_2@DOX@Cu/ZIF-8 decomposes to release CaO_2 and the fragments of the Cu/ZIF-8 MOF. CaO_2 reacts with H_2O_2 in the tumor cells in the presence of GSH to produce •OH, which then reacts with DPBF. Therefore, monitoring the change in absorbance at 410 nm was used to determine if CaO_2@DOX@Cu/ZIF-8 was responsive to GSH. To accomplish this, CaO_2@DOX@Cu/ZIF-8 NPs solutions were supplemented with GSH, H_2O_2, and DPBF by varying the incubation time to determine whether −OH was produced. As shown in Figure 3d, under normal

https://doi.org/10.1021/acsomega.3c00269
ACS Omega 2023, 8, 19402−19412

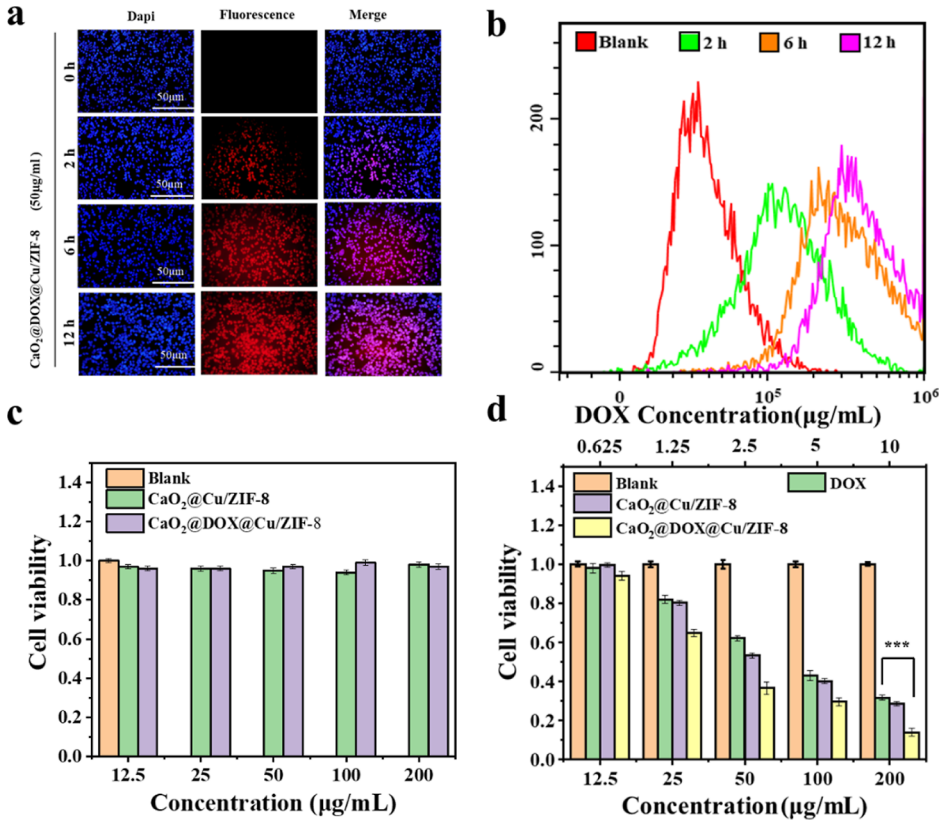

Figure 4. In vitro experiments with CaO_2@DOX@Cu/ZIF-8. (a) Fluorescence microscopy images demonstrating the cellular uptake of CaO2@DOX@Cu/ZIF-8 into HGC cells over time. (b) Flow cytometry analysis of the cells incubated with CaO_2@DOX@Cu/ZIF-8. (c) Cell viability of MEF cells treated with blank, CaO_2@Cu/ZIF-8, and CaO_2@DOX@Cu/ZIF-8 at different concentrations. (d) Cell viability of HGC cells treated with DOX, CaO_2@Cu/ZIF-8, and CaO_2@DOX@Cu/ZIF-8 at different concentrations. *P* values in panels (d) were calculated by Student's *t*-test; triple asterisks indicate $p < 0.001$.

physiological conditions, after the solution containing GSH, H_2O_2, and DPBF was supplemented with CaO_2@DOX@Cu/ZIF-8, with time increase, the absorbance at 410 nm did not change. However, in the simulated microenvironment of the tumor, the absorbance of DPBF at 410 nm gradually decreased with increasing incubation time, indicating that the DPBF reacted with the ROS generated from the components of CaO_2@DOX@Cu/ZIF-8 NPs after decomposition in the acidic medium (Figure 3e). In the simulated microenvironment of the tumor, the absorbance of DPBF at 410 nm was found to be almost unchanged when only CaO_2 was added (Figure S1), thus indicating that CaO_2@DOX@Cu/ZIF-8 NPs have the ability to release ROS in the tumor environment.

3.3. Extracellular Depletion of GSH. DTNB was used to detect whether CaO_2@DOX@Cu/ZIF-8 NPs were responsive to physiological levels of GSH. In the tumor microenvironment, CaO_2@DOX@Cu/ZIF-8 NPs will decompose to release Cu^{2+}, which will react with H_2O_2 to produce $^{\bullet}OH$ in the presence of GSH. Therefore, the response of CDT materials to GSH is essential. In the presence of sufficient GSH and H_2O_2 levels, Cu^{2+} can catalyze the conversion of GSH to GSSG. If the amount of glutathione peroxidase is sufficient and the rate-limiting factor of the reaction, there will be an appropriate amount of GSH left, and the remaining GSH will react with DTNB to form GSSG and 5-mercapto-2-nitrobenzoic acid, forming an absorption peak at 412 nm. Therefore, monitoring the change in the absorbance of the reaction solution at 412 nm was used to determine whether CaO_2@DOX@Cu/ZIF-8 reacted with GSH. As the concentration of CaO_2@DOX@Cu/ZIF-8 NPs increased from 0 to 80 μg/mL, the absorbance of the solution at 412 nm decreased continuously (Figure 3f), which indicated that the GSH content in the solution decreased rapidly, further demonstrating that CaO_2@DOX@Cu/ZIF-8 NPs had excellent GSH responsiveness.

3.4. Cellular Uptake and Toxicity In Vitro. The uptake of CaO_2@DOX@Cu/ZIF-8 NPs by cells was observed by fluorescence microscopy after incubation of HGC cells with CaO_2@DOX@Cu/ZIF-8 NPs (50 μg/mL) for 2, 4, 6, and 12 h. The cells were stained with DAPI, and the red fluorescence represents CaO_2@DOX@Cu/ZIF-8 NPs, while the nucleus was stained blue. Figure 4a shows that red fluorescence appeared in the cells after 2 h, indicating that CaO_2@DOX@Cu/ZIF-8 had entered the cells. As the time gradually increased to 12 h, the intensity of red fluorescence gradually increased with time, indicating that CaO_2@DOX@Cu/ZIF-8 NPs accumulated gradually in the cells over time. The flow cytometry results (Figure 4b) demonstrated that the fluorescence intensity of the dye in the HGC cells increased as the cell culture time increased, corroborating the staining patterns observed in the fluorescence microscopy images. Therefore, CaO_2@DOX@Cu/ZIF-8 NPs was taken up into the cells over time.

The toxicity of CaO_2@DOX@Cu/ZIF-8 in tumor cells and normal cells was assessed by CCK-8 assays. HGC cells were treated with PBS, DOX, CaO_2@Cu/ZIF-8, and CaO_2@DOX@Cu/ZIF-8, while the MEF cells (Mouse embryonic fibroblasts) were treated with PBS, CaO_2@Cu/ZIF-8, and CaO_2@DOX@Cu/ZIF-8. All cells were incubated for a total of

https://doi.org/10.1021/acsomega.3c00269
ACS Omega 2023, 8, 19402−19412

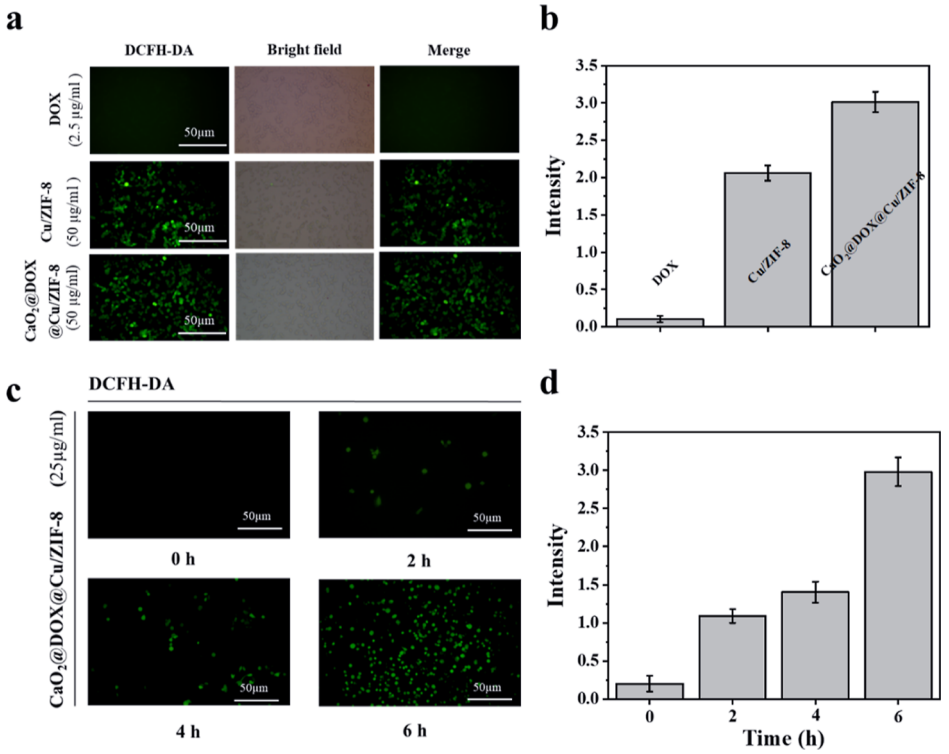

Figure 5. In vitro experiments with CaO_2@DOX@Cu/ZIF-8. (a,b) ROS production from DOX, Cu/ZIF-8, and CaO_2@DOX@Cu/ZIF-8 in HCG cells over time. (c,d) ROS production capacity of CaO_2@DOX@Cu/ZIF-8 in HCG cells over time.

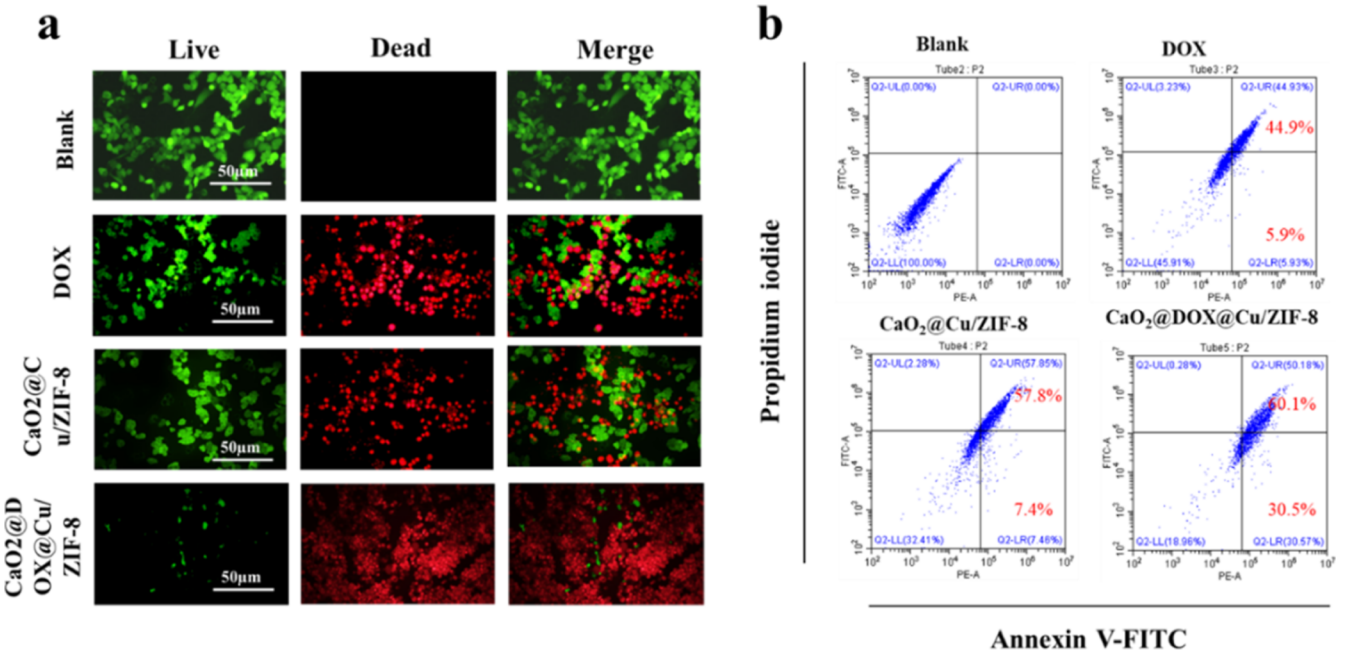

Figure 6. In vitro experiment of CaO_2@DOX@Cu/ZIF-8. (a) Live death analysis of DOX, CaO_2@Cu/ZIF-8, and CaO_2@DOX@Cu/ZIF-8 on tumor cells. (b) Apoptosis analysis of DOX, Cu/ZIF-8, and CaO_2@DOX@Cu/ZIF-8 on tumor cells.

24 h. As shown in Figure 4c, at a concentration of 200 μg/mL, the viability of the MEF cells co-incubated with CaO_2@Cu/ZIF-8 and CaO_2@DOX@Cu/ZIF-8 was greater than 90%, indicating that Cu/ZIF-8 was biocompatible and non-toxic. However, the viability of the HGC cells decreased with increased concentrations of nanomaterials (Figure 4d). CaO_2@DOX@Cu/ZIF-8 group had the greatest decrease in cell viability compared to the other materials. This suggested that CaO_2@DOX@Cu/ZIF-8 NPs had a more potent effect on the proliferation of the cancer cells compared to the other materials, as expected. The DOX, CaO_2@Cu/ZIF-8, and CaO_2@DOX@Cu/ZIF-8 corresponding IC_{50} values are calculated as in Table S1.

3.5. Intracellular •OH Production. To further investigate whether CaO_2@DOX@Cu/ZIF-8 NPs could generate ROS intracellularly, the DCFH-DA probe was employed to detect

https://doi.org/10.1021/acsomega.3c00269
ACS Omega 2023, 8, 19402−19412

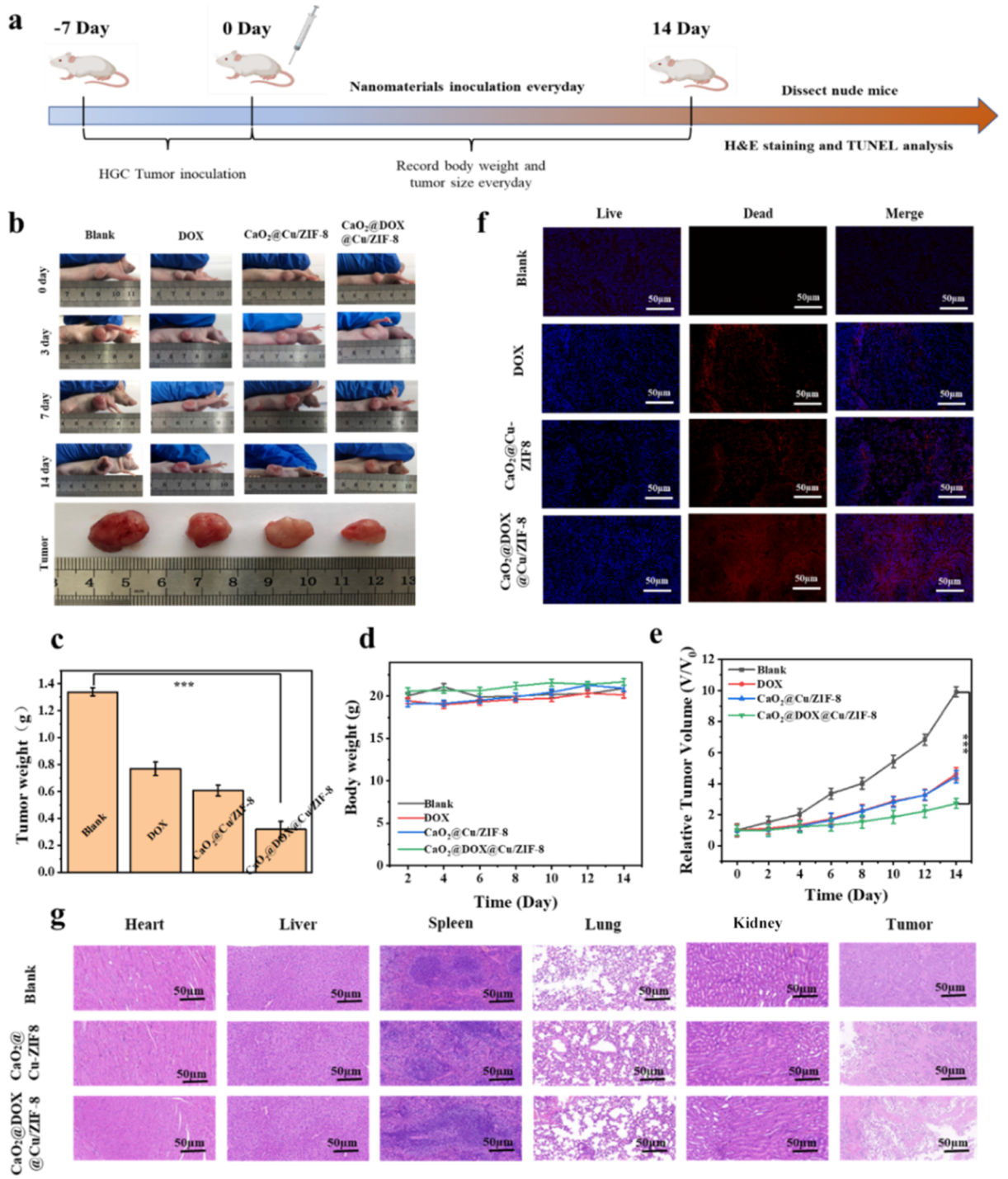

Figure 7. In vivo effects of CaO_2@DOX@Cu/ZIF-8 in Balb/c nude mice. (a) Flow chart of the in vivo experiments. (b) Tumor size changes during the 14 day treatment with PBS, DOX, CaO_2@DOX@Cu/ZIF-8, and CaO_2@DOX@Cu/ZIF-8. (c) Tumor weight after the treatment of the nude mice with PBS, DOX, CaO_2@DOX@Cu/ZIF-8, and CaO_2@DOX@Cu/ZIF-8. (d) Changes in body weight of the mice treated for 14 days with PBS, DOX, CaO_2@DOX@Cu/ZIF-8, and CaO_2@DOX@Cu/ZIF-8. (e) Changes in the relative tumor volume during the 14 day treatment period with PBS, DOX, CaO_2@DOX@Cu/ZIF-8, and CaO_2@DOX@Cu/ZIF-8. (f) TUNEL staining of the tumor tissues collected from nude mice. (g) H&E analysis of the major organs and tumor tissues collected from nude mice in each treatment group. *P* values in panels (c,e) were calculated by Student's *t*-test; triple asterisks indicate $p < 0.001$.

the production of ROS. Upon entry into cells, DCFH-DA is hydrolyzed by intracellular esterases to produce the non-fluorescent 2′,7′-dichlorodihydrofluorescein (DCFH). DCFH is readily oxidized by intracellular ROS, producing the fluorescent 2′,7′-dichlorofluorescein (DCF). Therefore, the levels of intracellular ROS can be determined by monitoring the change in the fluorescence. The fluorescence intensities of DCF in the cells treated with DOX, Cu/ZIF-8, and CaO_2@DOX@Cu/ZIF-8 were measured by inverted fluorescence microscopy and quantified from the microscopy images in the ImageJ software. The corresponding results are shown in Figure 5a,b. The Cu/ZIF-8- and CaO_2@DOX@Cu/ZIF-8-

https://doi.org/10.1021/acsomega.3c00269
ACS Omega 2023, 8, 19402−19412

treated cells had obvious fluorescence signals, indicating that the Cu/ZIF-8 decomposed to release Cu^{2+}, which reacted with H_2O_2 to generate $^{\bullet}OH$ in the tumor cells. These two groups produced stronger fluorescence signals than the cells treated with CaO_2@DOX@Cu/ZIF-8 under the same conditions, which was attributed to the fact that CaO_2 was released from the nanocomposite and reacted with water to generate a large amount of H_2O_2 in the tumor cells to convert DCFH to DCF. In addition, as shown in Figure 5c,d, there was a gradual increase in the fluorescence intensity of DCF in the cells treated with CaO_2@DOX@Cu/ZIF-8 NPs over time, indicating that CaO_2@DOX@Cu/ZIF-8 NPs demonstrated a sustained output of ROS. These results firmly demonstrated that CaO_2@DOX@Cu/ZIF-8 NPs could effectively generate ROS for enabling effective CDT in tumor cells.

3.6. Anticancer Activity In Vitro. PI and Calcein-AM dyes are widely used to assess cell viability after cells are treated with NPs because live cells fluoresce green and dead cells fluoresce red. As shown in Figure 6a, the cells treated with PBS (blank group) comprised nearly entirely green-fluorescing cells, indicating that most of the cells were alive. At the same drug concentration, some red fluorescence appeared in the field of view after cells were treated with DOX and CaO_2@Cu/ZIF-8 NPs, indicating that some cells underwent apoptosis after treatment. In contrast, there was almost no green fluorescence in the field of view after treatment of the cells with CaO_2@DOX@Cu/ZIF-8 NPs, indicating that most of the cells underwent apoptosis. Therefore, CaO_2@DOX@Cu/ZIF-8 NPs had the most significant killing effect on the tumor cells, which reflected the advantages of the combined CDT and chemotherapy in the treatment of cancer. It can also be seen from Figure 6b that the cell survival rate of the blank group was 100%, while the apoptosis rate of the DOX group was 50.8%. Furthermore, the apoptosis rate of CaO_2 @Cu/ZIF-8 NPs group was 64.8%, while the apoptosis rate of CaO_2@DOX@Cu/ZIF-8 NPs group was 80.6%.

3.7. Antitumor Effect In Vivo. After establishing the mouse tumor model and 14 consecutive days of treatment with the nanomaterials, the heart, liver, spleen, lungs, kidneys, and tumors were dissected from the nude mice (Figure 7a). Based on the photos (Figure 7b) and masses of the tumors (Figure 7c), the tumors dissected from the mice in the control group were the largest and heaviest, while the tumors dissected from the mice treated with CaO_2@DOX@Cu/ZIF-8 NPs were the smallest and lightest. As shown in Figure 7d, after continuous treatment for 14 days and weighing the nude mice daily, no significant changes in body weight between the CaO_2@DOX@Cu/ZIF-8-treated group and the blank group were observed. The tumors dissected from the mice treated with CaO_2@DOX@Cu/ZIF-8 NPs demonstrated the smallest volume change based on observation, indicating that CaO_2@DOX@Cu/ZIF-8 NPs were the most efficacious of the nanomaterials for inhibiting tumor growth (Figure 7e). To further investigate the efficacy of the nanomaterials in vivo, TUNEL analysis was performed on the tumors of nude mice treated with PBS, DOX, CaO_2@Cu/ZIF-8, and CaO_2@DOX@Cu/ZIF-8. Significantly higher levels of apoptosis were observed in the tumors derived from the mice treated with free DOX, CaO_2@Cu/ZIF-8, and CaO_2@DOX@Cu/ZIF-8 compared to the tumors derived from the mice treated with PBS, with the highest apoptosis rate being observed in the CaO_2@DOX@Cu/ZIF-8 group (Figure 7f). After H&E staining analysis of the tumor sections and major organs, the tumor cells in both CaO_2@Cu/ZIF-8NPs and CaO_2@DOX@Cu/ZIF-8NPs-treated mice had been destroyed, but the cells in the major organs remained normal, demonstrating that the CaO_2@DOX@Cu/ZIF-8 nanomaterial was able to selectively inhibit the growth of the HGC-based tumor without affecting normal cells (Figure 7g).

4. CONCLUSIONS

In this paper, we successfully fabricated a pH-sensitive, MOF-containing core−shell nanoplatform (CaO_2@DOX@Cu/ZIF-8). DOX was loaded onto the surface of CaO_2 NPs, onto which the Cu/ZIF-8 MOFs were layered. The Cu/ZIF-8 was used as a backbone to encapsulate CaO_2@DOX to form a TME-responsive, chemotherapeutic drug delivery system. Under acidic conditions (i.e., tumor microenvironment), CaO_2@DOX@Cu/ZIF-8NPs rapidly disintegrated to release Cu^{2+}, which reacted with H_2O_2 in the presence of GSH in a Fenton-like manner to produce highly cytotoxic $^{\bullet}OH$ radicals, thereby inducing oxidative stress and killing the cancer cells. The hydrolysis of intracellular CaO_2 produced H_2O_2, enhancing the CDT efficacy of the nanomaterials in cancer cells. It was demonstrated by cellular experiments that CaO_2@DOX@Cu/ZIF-8 enhanced the treatment of tumors by combining chemotherapy with CDT compared to a single treatment. The analysis of major organs and tumors in nude mice showed that CaO_2@DOX@Cu/ZIF-8 had a more pronounced tumor inhibition effect compared to other materials and excellent biocompatibility. Therefore, this nanocatalytic drug provides a new idea to realize the combination of chemotherapy and CDT to enhance the inhibition effect on tumors.

■ ASSOCIATED CONTENT

Supporting Information

The Supporting Information is available free of charge at https://pubs.acs.org/doi/10.1021/acsomega.3c00269.

Reactive oxygen test results and IC_{50} values of the DOX, CaO_2@Cu/ZIF-8, and CaO_2@DOX@Cu/ZIF-8 (PDF)

■ AUTHOR INFORMATION

Corresponding Author

Yugui Tao − *School of Biological and Food Engineering, Anhui Polytechnic University, Wuhu, Anhui 241000, People's Republic of China;* orcid.org/0000-0002-0144-4872; Email: swgctaoyg@126.com

Authors

Jie Liang − *School of Biological and Food Engineering, Anhui Polytechnic University, Wuhu, Anhui 241000, People's Republic of China*

Weiwei Zhang − *School of Biological and Food Engineering, Anhui Polytechnic University, Wuhu, Anhui 241000, People's Republic of China;* orcid.org/0000-0001-6141-9153

Jun Wang − *School of Biological and Food Engineering, Anhui Polytechnic University, Wuhu, Anhui 241000, People's Republic of China*

Wanzhen Li − *School of Biological and Food Engineering, Anhui Polytechnic University, Wuhu, Anhui 241000, People's Republic of China*

https://doi.org/10.1021/acsomega.3c00269
ACS Omega 2023, 8, 19402−19412

Fei Ge − *School of Biological and Food Engineering, Anhui Polytechnic University, Wuhu, Anhui 241000, People's Republic of China;* orcid.org/0000-0002-6308-3224
Weihao Jin − *School of Biological and Food Engineering, Anhui Polytechnic University, Wuhu, Anhui 241000, People's Republic of China*

Complete contact information is available at: https://pubs.acs.org/10.1021/acsomega.3c00269

Author Contributions

All authors contributed to the experimental procedure, data analysis, and manuscript revision.

Notes

The authors declare no competing financial interest.

■ ACKNOWLEDGMENTS

This work was supported by Anhui Provincial Higher Education Institutes (KJ2020A0375, KJ2021A0511, and KJ2020A118), the Youth Key Talents Program of Wannan Medical College (wyqnyx202005), the Youth Scientific Research Program of Wannan Medical College (WK2021F25), the Key Research and Development Program of Anhui Science and Technology Department (2022i01020002), and the Scientific Research Project of Anhui Polytechnic University (Xjky2022089).

■ REFERENCES

(1) Cao, C.; Wang, X.; Yang, N.; Song, X.; Dong, X. Recent advances of cancer chemodynamic therapy based on Fenton/Fenton-like chemistry. *Chem. Sci.* **2022**, *13*, 863−889.
(2) Cao, C.; Zou, H.; Yang, N.; Li, H.; Cai, Y.; Song, X.; Shao, J.; Chen, P.; Mou, X.; Wang, W.; Dong, X. Fe_3O_4/Ag/Bi_2MoO_6 Photoactivatable Nanozyme for Self-Replenishing and Sustainable Cascaded Nanocatalytic Cancer Therapy. *Adv. Mater.* **2021**, *33*, No. e2106996.
(3) Tang, Z.; Zhao, P.; Wang, H.; Liu, Y.; Bu, W. Biomedicine Meets Fenton Chemistry. *Chem. Rev.* **2021**, *121*, 1981−2019.
(4) Yang, L.; Jia, P.; Song, S.; Dong, Y.; Shen, R.; He, F.; Gai, S. On-Demand Triggered Chemodynamic Therapy by NIR-II Light on Oxidation-Prevented Bismuth Nanodots. *ACS Appl. Mater. Interfaces* **2022**, *14*, 21787−21799.
(5) Zhang, S.; Cao, C.; Lv, X.; Dai, H.; Zhong, Z.; Liang, C.; Wang, W.; Huang, W.; Song, X.; Dong, X. A H_2O_2 self-sufficient nanoplatform with domino effects for thermal-responsive enhanced chemodynamic therapy. *Chem. Sci.* **2020**, *11*, 1926−1934.
(6) Liu, X.; Zhang, M.; Yan, D.; Deng, G.; Wang, Q.; Li, C.; Zhao, L.; Lu, J. A smart theranostic agent based on Fe-HPPy@Au/DOX for CT imaging and PTT/chemotherapy/CDT combined anticancer therapy. *Biomater. Sci.* **2020**, *8*, 4067−4072.
(7) Kong, H.; Chu, Q.; Fang, C.; Cao, G.; Han, G.; Li, X. Cu-Ferrocene-Functionalized CaO_2 Nanoparticles to Enable Tumor-Specific Synergistic Therapy with GSH Depletion and Calcium Overload. *Adv. Sci.* **2021**, *8*, No. e2100241.
(8) Meng, Y.; Zhang, D.; Chen, X.; Dai, Z.; Yao, X.; Cui, P.; Yu, D.; Zhang, G.; Zheng, X. FePt Nanoparticles Embedded in Metal−Organic Framework Nanoparticles for Tumor Imaging and Eradication. *ACS Appl. Nano Mater.* **2020**, *3*, 4494−4503.
(9) Tian, H.; Zhang, M.; Jin, G.; Jiang, Y.; Luan, Y. Cu-MOF chemodynamic nanoplatform via modulating glutathione and H_2O_2 in tumor microenvironment for amplified cancer therapy. *J. Colloid Interface Sci.* **2021**, *587*, 358−366.
(10) Lin, L. S.; Huang, T.; Song, J.; Ou, X. Y.; Wang, Z.; Deng, H.; Tian, R.; Liu, Y.; Wang, J. F.; Liu, Y.; Yu, G.; Zhou, Z.; Wang, S.; Niu, G.; Yang, H. H.; Chen, X. Synthesis of Copper Peroxide Nanodots for H_2O_2 Self-Supplying Chemodynamic Therapy. *J. Am. Chem. Soc.* **2019**, *141*, 9937−9945.
(11) Zhang, K.; Meng, X.; Yang, Z.; Dong, H.; Zhang, X. Enhanced cancer therapy by hypoxia-responsive copper metal-organic frameworks nanosystem. *Biomaterials* **2020**, *258*, 120278.
(12) Su, M.; Zhang, R.; Li, H.; Jin, X.; Li, J.; Yue, X.; Qin, D. In situ deposition of MOF199 onto hierarchical structures of bamboo and wood and their antibacterial properties. *RSC Adv.* **2019**, *9*, 40277−40285.
(13) Wang, Y.; Wu, W.; Liu, J.; Manghnani, P. N.; Hu, F.; Ma, D.; Teh, C.; Wang, B.; Liu, B. Cancer-Cell-Activated Photodynamic Therapy Assisted by Cu(II)-Based Metal-Organic Framework. *ACS Nano* **2019**, *13*, 6879−6890.
(14) Wang, Y.; Wu, W.; Mao, D.; Teh, C.; Wang, B.; Liu, B. Metal−Organic Framework Assisted and Tumor Microenvironment Modulated Synergistic Image-Guided Photo-Chemo Therapy. *Adv. Funct. Mater.* **2020**, *30*, 2002431.
(15) Hao, Y.; Gao, Y.; Fan, Y.; Zhang, C.; Zhan, M.; Cao, X.; Shi, X.; Guo, R. A tumor microenvironment-responsive poly(amidoamine) dendrimer nanoplatform for hypoxia-responsive chemo/chemodynamic therapy. *J. Nanobiotechnol.* **2022**, *20*, 43.
(16) Ding, Y.; Xu, H.; Xu, C.; Tong, Z.; Zhang, S.; Bai, Y.; Chen, Y.; Xu, Q.; Zhou, L.; Ding, H.; Sun, Z.; Yan, S.; Mao, Z.; Wang, W. A Nanomedicine Fabricated from Gold Nanoparticles-Decorated Metal-Organic Framework for Cascade Chemo/Chemodynamic Cancer Therapy. *Adv. Sci.* **2020**, *7*, 2001060.
(17) Zhang, L.; Li, G.; Ouyang, Z.; Yang, R.; Gao, Y.; Cao, X.; Banyai, I.; Shi, X.; Guo, R. Intelligent design of iron-doped LDH nanosheets for cooperative chemo-chemodynamic therapy of tumors. *Biomater. Sci.* **2022**, *10*, 2029−2039.
(18) Liu, C.; Li, M.; Liu, C.; Qiu, S.; Bai, Y.; Fan, L.; Tian, W. A supramolecular organometallic drug complex with H_2O_2 self-provision intensifying intracellular autocatalysis for chemodynamic therapy. *J. Mater. Chem. B* **2022**, *10*, 8981−8987.
(19) Wang, Z.; Liu, B.; Sun, Q.; Dong, S.; Kuang, Y.; Dong, Y.; He, F.; Gai, S.; Yang, P. Fusiform-Like Copper(II)-Based Metal−Organic Framework through Relief Hypoxia and GSH-Depletion Co-Enhanced Starvation and Chemodynamic Synergetic Cancer Therapy. *ACS Appl. Mater. Interfaces* **2020**, *12*, 17254−17267.
(20) Zou, B.; Xiong, Z.; He, L.; Chen, T. Reversing breast cancer bone metastasis by metal organic framework-capped nanotherapeutics via suppressing osteoclastogenesis. *Biomaterials* **2022**, *285*, 121549.
(21) Zhou, Y.; Fan, S.; Feng, L.; Huang, X.; Chen, X. Manipulating Intratumoral Fenton Chemistry for Enhanced Chemodynamic and Chemodynamic-Synergized Multimodal Therapy. *Adv. Mater.* **2021**, *33*, No. e2104223.
(22) Wang, Z.; Guo, Y.; Fan, Y.; Chen, J.; Wang, H.; Shen, M.; Shi, X. Metal-Phenolic-Network-Coated Dendrimer-Drug Conjugates for Tumor MR Imaging and Chemo/Chemodynamic Therapy via Amplification of Endoplasmic Reticulum Stress. *Adv. Mater.* **2022**, *34*, No. e2107009.
(23) Qian, M.; Cheng, Z.; Luo, G.; Galluzzi, M.; Shen, Y.; Li, Z.; Yang, H.; Yu, X. F. Molybdenum Diphosphide Nanorods with Laser-Potentiated Peroxidase Catalytic/Mild-Photothermal Therapy of Oral Cancer. *Adv. Sci.* **2022**, *9*, 2101527.
(24) Qi, C.; He, J.; Fu, L. H.; He, T.; Blum, N. T.; Yao, X.; Lin, J.; Huang, P. Tumor-Specific Activatable Nanocarriers with Gas-Generation and Signal Amplification Capabilities for Tumor Theranostics. *ACS Nano* **2021**, *15*, 1627−1639.
(25) Kang, Y.; Yu, X.; Fan, X.; Aodenggerile; Zhao, S.; Tu, C.; Yan, Z.; Wang, R.; Li, W.; Qiu, H. Tetramodal Imaging and Synergistic Cancer Radio-Chemotherapy Enabled by Multiple Component-Encapsulated Zeolitic Imidazolate Frameworks. *ACS Nano* **2020**, *14*, 4336−4351.
(26) Deng, T.; Luo, D.; Zhang, R.; Zhao, R.; Hu, Y.; Zhao, Q.; Wang, S.; Iqbal, M. Z.; Kong, X. DOX-loaded hydroxyapatite nanoclusters for colorectal cancer (CRC) chemotherapy: evaluation based on the cancer cells and organoids. *SLAS Technol.* **2023**, *28*, 22−31.
(27) Gao, S.; Jin, Y.; Ge, K.; Li, Z.; Liu, H.; Dai, X.; Zhang, Y.; Chen, S.; Liang, X.; Zhang, J. Self-Supply of O_2 and H_2O_2 by a Nanocatalytic

Medicine to Enhance Combined Chemo/Chemodynamic Therapy. *Adv. Sci.* **2019**, *6*, 1902137.
(28) Zeng, R.; He, T.; Lu, L.; Li, K.; Luo, Z.; Cai, K. Ultra-thin metal-organic framework nanosheets for chemo-photodynamic synergistic therapy. *J. Mater. Chem. B* **2021**, *9*, 4143−4153.
(29) Zhao, L.; Fu, C.; Tan, L.; Li, T.; Zhong, H.; Meng, X. Advanced nanotechnology for hypoxia-associated antitumor therapy. *Nanoscale* **2020**, *12*, 2855−2874.
(30) Sheng, Y.; Nesbitt, H.; Callan, B.; Taylor, M. A.; Love, M.; McHale, A. P.; Callan, J. F. Oxygen generating nanoparticles for improved photodynamic therapy of hypoxic tumours. *J. Controlled Release* **2017**, *264*, 333−340.
(31) Thi, P. L.; Lee, Y.; Tran, D. L.; Hoang Thi, T. T.; Park, K. M.; Park, K. D. Calcium peroxide-mediated in situ formation of multifunctional hydrogels with enhanced mesenchymal stem cell behaviors and antibacterial properties. *J. Mater. Chem. B* **2020**, *8*, 11033−11043.
(32) Han, Y.; Ouyang, J.; Li, Y.; Wang, F.; Jiang, J. H. Engineering H_2O_2 Self-Supplying Nanotheranostic Platform for Targeted and Imaging-Guided Chemodynamic Therapy. *ACS Appl. Mater. Interfaces* **2020**, *12*, 288−297.
(33) Sun, Q.; Liu, B.; Zhao, R.; Feng, L.; Wang, Z.; Dong, S.; Dong, Y.; Gai, S.; Ding, H.; Yang, P. Calcium Peroxide-Based Nanosystem with Cancer Microenvironment-Activated Capabilities for Imaging Guided Combination Therapy via Mitochondrial Ca^{2+} Overload and Chemotherapy. *ACS Appl. Mater. Interfaces* **2021**, *13*, 44096−44107.
(34) Wang, H.-Y.; Su, Z.-C.; He, X.-W.; Li, W.-Y.; Zhang, Y.-K. H_2O_2 self-supplying degradable epitope imprinted polymers for targeted fluorescence imaging and chemodynamic therapy. *Nanoscale* **2021**, *13*, 12553−12564.
(35) Khorshidi, S.; Karkhaneh, A.; Bonakdar, S. Fabrication of amine-decorated nonspherical microparticles with calcium peroxide cargo for controlled release of oxygen. *J. Biomed. Mater. Res., Part A* **2020**, *108*, 136−147.
(36) Hu, C.; Yu, Y.; Chao, S.; Zhu, H.; Pei, Y.; Chen, L.; Pei, Z. A Supramolecular Photosensitizer System Based on Nano-Cu/ZIF-8 Capped with Water-Soluble Pillar[6]arene and Methylene Blue Host-Guest Complexations. *Molecules* **2021**, *26*, 3878.
(37) Xie, Z.; Liang, S.; Cai, X.; Ding, B.; Huang, S.; Hou, Z.; Ma, P.; Cheng, Z.; Lin, J. O_2-Cu/ZIF-8@Ce6/ZIF-8@F127 Composite as a Tumor Microenvironment-Responsive Nanoplatform with Enhanced Photo-/Chemodynamic Antitumor Efficacy. *ACS Appl. Mater. Interfaces* **2019**, *11*, 31671−31680.

https://doi.org/10.1021/acsomega.3c00269
ACS Omega 2023, 8, 19402−19412